Lab on a Chip

Accepted Manuscript

This is an *Accepted Manuscript*, which has been through the Royal Society of Chemistry peer review process and has been accepted for publication.

Accepted Manuscripts are published online shortly after acceptance, before technical editing, formatting and proof reading. Using this free service, authors can make their results available to the community, in citable form, before we publish the edited article. We will replace this *Accepted Manuscript* with the edited and formatted *Advance Article* as soon as it is available.

You can find more information about *Accepted Manuscripts* in the **Information for Authors**.

Please note that technical editing may introduce minor changes to the text and/or graphics, which may alter content. The journal's standard **Terms & Conditions** and the **Ethical guidelines** still apply. In no event shall the Royal Society of Chemistry be held responsible for any errors or omissions in this *Accepted Manuscript* or any consequences arising from the use of any information it contains.

Graphical abstract

We present a thorough experimental and theoretical analysis of nanoscale electrokinetics using ion-selective nanochannel networks formed by geometrically controlled *in situ* self-assembled nanoparticles.
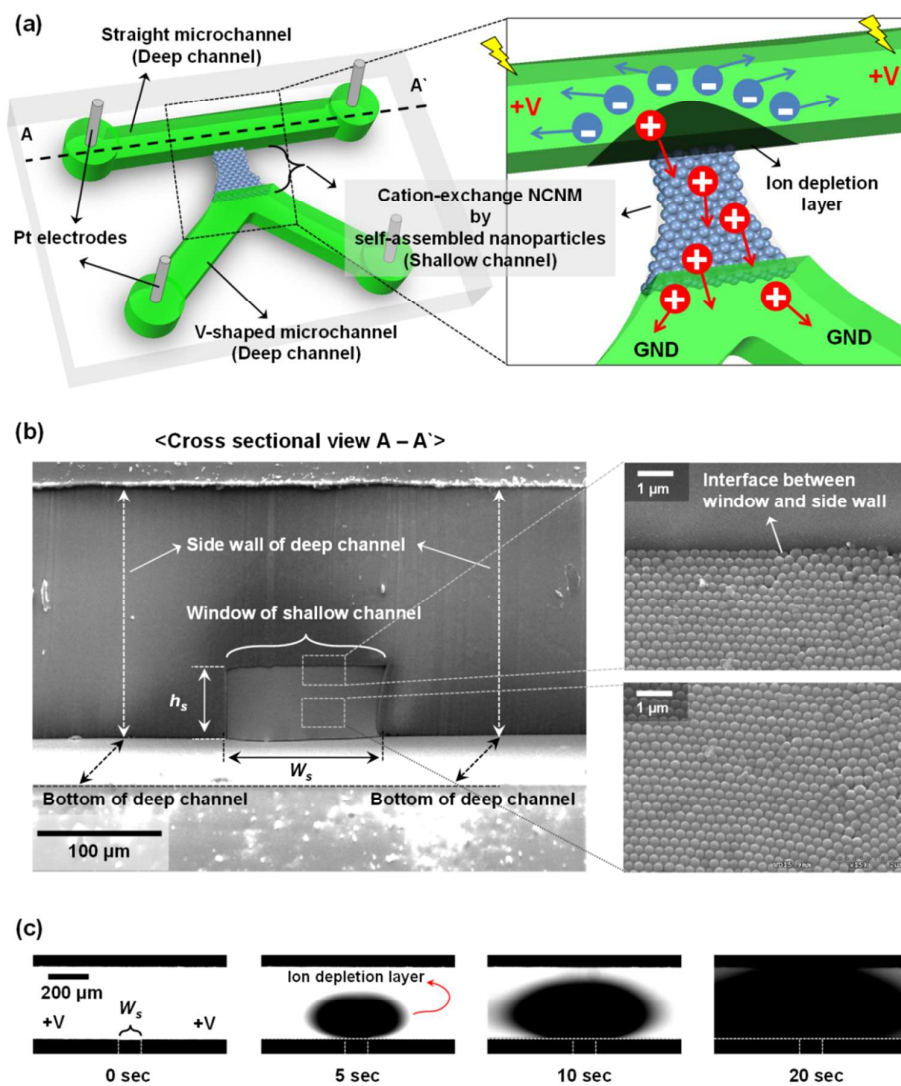
Electrokinetic Study on Tunable 3D Nanochannel Networks Constructed by Spatially Controlled Nanoparticle Assembly†

Eunpyo Choi,[1] Kilsung Kwon,[1] Daejoong Kim,[1,*] and Jungyul Park[1,*]

[1]Department of Mechanical Engineering, Sogang University, 35 Baekbeom-ro, Mapo-gu, Seoul, 121-742, Korea

[*]Correspondence should be addressed to Prof. Jungyul Park and Prof. Daejoong Kim:

E-mail: sortpark@sogang.ac.kr, daejoong@sogang.ac.kr

1

ABSTRACT

This paper proposes a novel method to form ion-selective nanochannel networks between two microfluidic channels using geometrically controlled *in situ* self-assembled nanoparticles. We present a thorough experimental and theoretical analysis of nanoscale electrokinetics using the proposed microplatform. The nano-interstices between these assembled nanoparticles serve as the nanopores of ion-selective membranes with the equivalent pore size. Its inherent characteristics (compared with the conventional one-dimensional nanochannels) are a high ionic flux and a low fluidic resistance because these nanopore clusters have a role as the collective three-dimensional nanochannel networks, which result in a highly efficient performance beneficial for various applications. Another uniqueness of our system is that the electrical characteristics (such as ion transport through the nanochannel networks and the decrease of the limiting current region) can be tuned quantitatively or even optimized by changing the geometry of the microchannel and the pH condition of the working solution or by properly selecting the size and materials of the assembled nanoparticles. The correlation between these tuning parameters and nanoscale electrokinetics is deeply investigated with carefully designed experiments and their mechanism is thoroughly examined by a theoretical study. We expect that the presented system and methodology can contribute to opening new application fields, such as biomolecule separation/filtering/accumulation/analysis, bioelectronics, and energy generation.

KEYWORDS

Concentration polarization, nanofluidic, nanoparticles, electrokinetics, ion-selective membrane.

2

INTRODUCTION

Background

The transport of ions through nanoscale geometries whose critical dimension is on the order of 10 to 100 nanometers such as nanopore clusters and nanochannels has been intensively studied in the recent decade owing to the advancement in micro- and nanofabrication.[1-4] The electrokinetic properties at this scale have intrigued research applications including chemical mixing,[5, 6] energy harvesting,[7-12] biomolecule concentration[13, 14] and separation,[15] water desalination and purification,[16] nanofluidic transistors,[17] ionic diodes,[18] *etc*. Most devices in diverse studies on nanofluidic electrokinetics have similar structures, that is, two microfluidic channels are physically interconnected with nanofluidic channels as a nanojuction. Recently, various nanojunctions are employed such as polymeric ion-exchange membranes (Nafion®[10, 13, 14, 16, 19] or Neocepta®[20-22]), porous hydrogel membranes,[23, 24] bulk-machined nanochannels in a glass or silicon wafer substrate,[1, 5-7, 15, 25-28] and ion track-etched nanopores.[8, 9, 18, 29, 30] However, these reported nanojunctions have several disadvantages; in the case of polymeric membranes and porous hydrogel, it is hard to control the geometries, for example, a pore size, its shape, and the location in the microfluidic channels. Also, these are not robust without aqueous environments and change their volume according to the level of water absorption. In other types of nanojunctions, the e-beam lithography-based nanochannels and ion track-etched nanopores require extensive fabrication processes and/or expensive and specialized equipment.

One of the challenging problems in aforementioned nanojunctions, especially for the application in micro total analysis systems (MicroTAS), is low ionic flux and high fluidic resistance of the junctions. This problem is especially evident in ion concentration polarization (ICP),[31] which is induced by perm-selective transport through the nanojunctions. ICP has been

3

widely utilized in chemical mixing,[5, 6] biomolecule concentration[13, 14] and separation,[15] water desalination and purification,[16] etc. To achieve high efficiency of ICP phenomena in these applications, it is desirable to obtain higher ionic flux and low fluidic resistance. Similarly, in energy harvesting from concentration gradient by reverse electrodialysis (RED), the fast ionic diffusion and higher ionic flux through the nanojunctions are required for high power and energy conversion efficiency. Due to these requirements, many researchers have tried to increase the ionic flux or reduce the fluidic resistance by multiple-arraying the nanochannels or nanopores[3, 5-9, 32] and changing the surface charge properties of the nanojunctions.[2, 33, 34] These approaches still have issues like the following. The array of nanochannels should be realized in two dimensions (2D), because of the intrinsic limitation of a top-down fabrication process, and it requires additional complicated fabrications or chemical modification processes for changing the surface charge properties due to the limited material availability. The material of nanochannels and ion track-etched nanoporous membranes are rather confined to silica and organic polymers, respectively.

In previous study, we proposed the chemical gradients generator using the micro-sized channel networks from the self-assembly of micro-sized particles.[35] The stable chemical gradient could be realized by allowing the transport of both ions and molecules through the micro-interstices which formed in the closed-packed microparticles. Now, we present nano-sized channel networks which have ion-selectivity. These are created between two microfluidic channels using geometrically controlled *in situ* self-assembled nano-sized particles in a cost-effective and simple fabrication fashion. Chen and co-workers[36] studied nanofluidic electrokinetics using the assembled nanoparticles in one straight PDMS channel, but this method is impossible to locate the nanoparticle assembly in desired area and shape. Hence, it is difficult to visualize ion

transport using fluorescent dye at the interface between microchannel and nanochannels, and to study the variation of electrokinetics by changing the geometry of microchannels, and even more to integrate with other components in MicroTAS for further applications. The proposed system is expected to achieve high ionic flux, because the nano-interstices between the assembled nanoparticles function as the collective three-dimensional (3D) nanochannel networks compared to the conventional nanochannel corresponding to a thin one-dimensional pathway. Another advantage of our system is that the electrical performance can be tuned quantitatively or even optimized by changing the geometry of the microchannel (tuning the ionic flux and eliminating the limiting current), properly selecting the nanoparticle size (tuning the ionic flux), choosing materials of the assembled nanoparticles (tuning the ionic flux and the different polarity), and/or even by modulating the value of the pH (tuning the ionic flux).

Working principle

    Fig. 1(a) shows the configuration of the proposed microplatform and the working principle of the ICP phenomena in this microplatform. The shallow channel between the two deep channels is fully filled with the self-assembled nanoparticles in a face centered cubic (FCC) structures. The nano-interstices formed in these closed-packed nanoparticles of homogeneous sizes, which consist of equivalent nanopores (~15 % of the sphere size),[37] serve as the pores of ion-selective membranes at a low ionic strength, because the so-called Debye layer thickness (λ_D) is comparable with the size of the nanopores in these nano-interstices.[27, 38] Here, we use these nanopore clusters as ion-selective membranes, which are stacked in 3D with interconnection with one another, and we will call this as "nanochannel networks membrane (NCNM)" through this paper. When a DC voltage is applied in the case of a cation-exchange NCNM (Fig. 1(a)), for

5

example, the ICP phenomenon occurs near the membrane as follows.[24, 26, 39] At the anodic side, positive ions can transport into the perm-selective NCNM but negative ions are expelled from the NCNM by the DC voltage. The condition of overall electro-neutrality forces the concentrations of both cations and anions to decrease in the anodic side of the NCNM and induce a concentration gradient. Because of this concentration gradient, a preferential cation transport through NCNM is satisfied across the entire system while maintaining a net zero anion flux. The ion transport and concentration are limited in the boundary region (diffusion layer) near the NCNM surface. As the DC voltage increases, the ion current increases with a fixed diffusion length and bulk concentration. Therefore, the system responds by decreasing the local ion concentration on the anodic side of the membrane (known as the ion-depletion phenomenon).

When the concentration approaches zero on the anodic side of the NCNM, the system reaches a limiting current. If the potential is further increased, the current can be extended beyond the limiting current. This overlimiting current can be observed in most perm-selective membranes. Rubinstein and co-workers[40-44] theoretically explained the overlimiting current phenomena. They suggested that the electro-convection is created by the amplified electrokinetic response of a fluid layer right next to the membrane. From the viewpoint of electro-convection, Dunkhin and Mishchuk[45-49] have been studied this physical origin of strong convective mixing with their terms of "first" kind and "second" kind of electro-osmosis. This convective mixing destroys the concentration polarization to cause overlimiting conduction. Also, in microfluidic systems, it can be effectively suppressed and hence the diffusion layer could be extended all the way back to the reservoir.[26] In characterizing electrokinetics through the proposed NCNM, we observe the extension of the diffusion layer and measure the ionic current density through the NCNM in

response to the size of nanoparticles, the geometry of the microchannel, the different values of the pH, and the material of the nanoparticles.

MATERIALS AND METHODS

Fabrication process of PDMS microfluidic channel

The PDMS microfluidic chip was fabricated using a standard soft lithography. The details of the fabrication process are provided in **Fig. S1 in ESI†**. Briefly, Fig. S1(a) to (e)† show the fabrication process with a multilayered design: (a) A 4 inch silicon wafer was patterned with a SU-8 negative photoresist. The height of the first layer for the shallow channel that can form the desired patterns for nanochannel networks was adjusted from 5 μm to 100 μm. Subsequently, SU-8 2050 was patterned on the first SU-8 layer (target: 100 μm, this layer is for the deep channel) (b) The PDMS mixture was poured onto the master and cured at 95°C for 1 h. (c) The PDMS was then peeled off. (d) Finally, it was bonded with a slide glass after O_2 plasma treatments.

In situ formation of nanochannel networks using nanoparticles

We formed the nanochannel networks using nanoparticles within the shallow channel, as reported previously.[35] **Fig. 1(b)** shows the fabrication process for the *in situ* formation of the nanochannel networks using the self-assembly of nanoparticles within the PDMS channel: (I) the PDMS device with the shallow and deep channels was fabricated as described above. (II) In this paper, we used the silica (SiO_2) nanospheres (100, 200, 300, and 700 nm of the diameters (D_n)), polystyrene (PS), and titanium oxide (TiO_2) nanospheres (D_n: 300 nm). The SiO_2 nanospheres (S-NPs) with D_n = 100, 300, 700 nm and PS nanospheres (PS-NPs) were purchased from

Polyscience Inc., USA, and $D_n = 200$ nm of SiO_2 nanospheres, and TiO_2 nanospheres (T-NPs) were obtained from Microspheres-Nanospheres Co., USA. 100 μL of the diluted nanoparticle solutions were centrifuged and re-suspended in 100 μL of the 50 % ethanol (v/v) solution. Subsequently, 2 μL of this solution was introduced into the deep channels by a capillary pressure. (III) The diluted nanoparticles at the intersection between the shallow and the deep channel experience a sudden pressure drop (ΔP_{12}), which drives the solution from the deep channel to the shallow channel ($F_{shallow}$).[50] (IV, V) In the designed horn-shaped channel, the self-assembly of the particles occurred uni-directionally since efficient evaporation and capillary pressure are induced at the narrow opening. However, this flow of the diluted nanoparticles in the shallow channel could not move forward toward the opposite sides of deep channel because, since the height was expended at the deep channel on the opposite side. While the expansion angle β was around 90°,[51] the capillary stop pressure was maximized. (VI) During the time the solution was dried out, the nanoparticles were self-assembled uni-directionally and the nanopores were formed as the nano-interstices in these closed-packed nanoparticles only within the shallow channel.

Experimental procedure

The potassium chloride (KCl, Sigma-Aldrich, USA) electrolyte solution was prepared by dissolving a target solute in deionized (DI) water. A precise scale (AB 264-S/31, Mettler Toredo, Switzerland) with the resolution of 0.01 mg was utilized to accurately meter the concentration of the electrolyte solutions. We measured the pH for the electrolyte solutions using a pH meter (SevenMulti[TM] S47, Mettler Toredo, Switzerland). In the experiment, the concentration of KCl solution at 0.1 mM was used and the value of pH was adjusted by adding the HCl or KOH

(Sigma-Aldrich, USA). In addition, we disregard the pH drift by the water splitting within the NCNM which bring the production of the hydronium (H^+) and the hydroxide (OH^-) in the overlimiting current region. Earlier researches have been claimed that the water splitting have a more significant role on the overlimiting current region in the *I-V* characteristics of the anion-exchange membrane than the cation-exchange membrane.[40, 52-56] The reason is that an increase in the water dissociation reaction rate constant is smaller for a cation-exchange membrane than for an anion-exchange membrane.[54-56] In our experiment conditions, all cases except the TiO_2 nanoparticles case, the NCNM plays the role as the cation-exchange. Furthermore, since we paid much attention to propose a new approach to form the nanochannel and to demonstrate the possibility of the advantages, we focused on the low current density region (Ohmic/ limiting current and limiting/overlimiting current transition region) rather than the high current density region (overlimiting current region) in the *I-V* characteristics. Therefore, we believe that the water splitting may have a negligible influence on these *I-V* characteristic regions. In case of the TiO_2 nanoparticles at pH 4.2, the NCNM acts like the anion-exchange membrane and the water splitting may occur if the voltage for high current density is maintained. However, in spite of the water splitting issue should be addressed, we observed the stable growth of the depletion layer within 40 sec at -30 V of the voltage to show the negative potential that the NCNM with the TiO_2 nanoparticles at pH 4.2 is working.

Moreover, we tried to reduce the local pH drift from the electrolysis near the electrodes and its effect to the bulk solution:[57] We used the KCl solution with low conductivity (0.1 mM concentration) for whole experiment and platinum (Pt) electrodes which have chemically stable. Moreover, we increase the reservoir size by inserting the pipet tip into the reservoir to confine the reaction zone. The reservoir itself in PDMS device has about 9 μl volumes. However, we

inserted the 200 µl containable pipet tip (T-200-Y, Axygen[TM], Thermo Fisher Scientific Inc.) into the reservoir, and then we filled the 100 µl of KCl solution into this pipet. Macka et. al.[58] reported that the changes of less than ±0.3 pH was observed 1 mm laterally from the electrode and/or at least 1mm vertically below the electrode end. Here, they applied the voltage of 20 kV to 30 kV, and used the un-buffered sodium chromate of 5 mM. However, in our conditions, the applied voltage is 1000-fold lower and NCNM is 40 mm away from the electrode. Therefore, we believed that pH drift from the electrolysis at the electrode and its effect to NCNM is negligible.

Another concerned problem in pH drift is water uptake of atmospheric carbon dioxide (CO_2) to form carbonic acid, which dissociates to successively form bicarbonate and carbonate ions, especially pH > 5.5.[59] In case of the experiment for the controlling of the particle size and the geometry, and the selecting the material for silica nanoparticles and polystyrene nanoparticles at pH 4.0 - 5.6, and TiO_2 nanoparticles at pH 4.2, we disregard the water uptake of CO_2 because an air-equilibrated pH value of the aqueous solution is about 5.6 and for pH < 5.5, the dissociation of CO_2 can be negligible.[59, 60] However, for PS-NPs at pH 9.4, carbonic acid concentration will increase as time goes by. To reduce this water uptake of CO_2, we let the electrolyte solutions cool down enough after dissolution and kept them sealed at the room temperature before the experiments. Then we performed the experiment immediately after prepared KCl solution and re-prepared the solution freshly for each experiment.

Fluorescein isothiocyanate (FITC , Sigma-Aldrich, USA) with negative charges or Rhodamine 6G (R6G, Sigma-Aldrich, USA) with positive charges were added to visualize the ion depletion layer and the onset time (time required for the ion depletion layer to reach 297 µm from the initial established point of its layer). The motions of the fluorescent dyes were monitored using

an inverted microscope (IX7, Olympus Co., Japan) and the images were recorded on a PC using a CCD camera (CoolSNAP, Photometrices, USA) installed in the microscope setup.

The voltage from a source meter (2400, Keithley Instrument, USA) was applied through platinum electrodes and it was controlled by a general purpose interface bus (GPIB, PCI-GPIB, National Instruments, USA) and Labview 9.0 (National Instruments, USA). The voltage signal and current signal were recorded in the computer connected to the voltage source through the GPIB card. In all the experiments, we obtained each $I\text{-}V$ curve in a galvanostatic mode and the voltages are applied from 0 to 15 V in the steps of 0.5 V every 1 sec. We repeated the experiment and plotted the $I\text{-}V$ curve with the error bars (standard error, more details in Sec. II of ESI†). For the onset times, the value of +30 V or -30 V of the DC voltage was applied.

In order to characterize the formation of the ion depletion layer according to different geometries of the shallow channel, the various heights (h_s: 5, 10, 50, and 100 μm) and the widths (w_s: 25, 50, 100, 200, and 400 μm) were used under the following conditions. The silica nanoparticles (S-NPs) with D_n = 300 nm and, FITC solution containing 0.1 mM KCl with pH 5.6 were used. For measuring the onset time with respect to different diameters of nanoparticles, the S-NPs with D_n = 100, 200, 300, 700 nm were used with the same FITC solutions as above. Moreover, the dynamic ion depletion layer formations were observed with various materials for the nanoparticles. The S-NPs of D_n = 300 nm and the same-sized polystyrene nanoparticles were used under the condition of the FITC solution with 0.1 mM KCl solution at pH 5.6 and 9.4. TiO_2 nanoparticles with the same diameter were used under the following conditions At the value of pH 4.2, the R6G dissolved in the electrolytes was used with the positive DC voltage and at the value of pH 9.1, the FITC in the electrolytes was used and the negative DC voltage was applied.

RESULTS AND DISCUSSIONS

Fig. 2(a) shows the fabricated microplatform and its enlarged microscopic images of the interface between the shallow and the deep channels. **Fig. 2(b)** shows the cross-sectional SEM images of the fabricated device along the A-A' direction in **Fig. 2(a)**. The inset shows the enlarged image of the interface between the window of the shallow channel and the side wall of the deep channel, and the middle of the window of the shallow channel. Interestingly, the crystallized nanoparticles do not extend further beyond the interface between the shallow and deep channels, which we intended originally. When we triggered the ICP in this microplatform, the ion depletion layer is established on the anodic side of the NCNM and it grows over time as shown in **Fig. 2(c)** as well as in the supplementary movie†. The silica nanoparticles (S-NPs) are 300 nm in diameter in the cation-exchange NCNM and we used a negatively charged fluorescein isothiocyanate (FITC) solution under the condition of 0.1 mM KCl (corresponding to λ_D of 30.4 nm) at the pH value of 5.6 for the visualization purpose.

To further investigate the effect of the NCNM on the ICP, we first observed the change in the onset time (time required for the ion depletion layer to reach 297 µm from the initial point of this layer) while varying the nanoparticle sizes as indicated in **Fig. 3(a)**. The onset times tend to decrease as the size is reduced from the diameters of 700 nm to 200 nm. We think the reason is as follows. Zangle and co-workers[31, 61, 62] claimed that the depletion layer will propagate as shock waves if the ratio of bulk to surface conductance ($c_{0,r}^{*}h_{n}^{*}$) is lower than the unity, *i.e.*, $c_{0,r}^{*}h_{n}^{*} = (\mu_{+}z_{+} - \mu_{-}z_{-})Fh_{n}c_{0,r}/(-2\mu_{+}\sigma) << 1$. However, If $c_{0,r}^{*}h_{n}^{*} >> 1$, there is no effects of propagating ICP. Here, $c_{0,r}$ is the background electrolyte concentration in reservoir (0.1 mM KCl); h_{n} is the height of the nanochannel (when the diameter of nanoparticle is 200, 300, and 700 nm, h_{n} is 30, 45, and 105 nm, respectively); μ_{+} and μ_{-} are the motilities of the positive and

12

negative ions ($\mu_{K^+} \approx 7.62 \times 10^{-8} \, m^2 V^{-1} s^{-1}$, $\mu_{Cl^-} \approx 7.19 \times 10^{-8} \, m^2 V^{-1} s^{-1}$);[63, 64] z_+ and z_- are the valence of the positive and negative ions (z_+, z_- = 1, -1); F is the Faraday constant (96485 C·mol^{-1}); σ is the surface charge density of nanochannel. Qian and co-workers[65-68] suggested the the surface charge density of particle, σ, based on the full multi-ion charge-regulation model. This developed analytical model can be used to predict the surface charge properties including both the surface charge density and the zeta potential of nanoparticles as function of the solution properties (*i. e.*, pH and background salt concentration).[66] The surface charge density can be expressed as $\sigma_A^* = -FN_{total}\{[K_A - K_B\Omega^2]/[K_A + \Omega + K_B\Omega^2]\}$. Here, Stern layer effect is neglected; N_{total} is the total site density of silanol functional groups on the particle surface; K_A and K_B are the equilibrium constants for the surface reactions, SiOH $\leftrightarrow$ SiO$^-$ + H$^+$ and SiOH + H$^+$ $\leftrightarrow$ SiOH$_2^+$, respectively; $\Omega = 10^{-pH} \exp(-F\zeta/R_gT)$; ζ is the measured zeta potential (-40.3 mV for S-NPs); R_g is the universal gas constant (8.314 J·Kg^{-1}·K^{-1}); T is the absolute temperature (298.15 K). When we consider a monovalent background electrolyte solution, such as 0.1 mM KCl with pH 5.6, and the silicon dioxide with N_{total} = 8 × 10^{-6} mol·m^{-2}, pK_A = -log K_A = 6.8, and pK_B = -log K_B = 1.9,[65, 69] the surface charge density can be estimated as -0.01013 C·m^{-2}. This value is reasonable agreement with the reference values, such as 0.018 C·m^{-2},[36] and 0.025 C·m^{-2}.[70] Therefore, at nanoparticle diameter with 700, 300 and 200 nm, $c_{0,r}^* h_n^*$ is about 0.099, 0.042, and 0.028, respectively. These results mean that when the nanoparticle size decrease, the propagation of depletion layer is promoted with decrease of the onset time. Moreover, when $c_{0,r}^* h_n^*$ decrease as the diameter is reduced, there can be much greater concentration of the potassium ions (positive ion) than chloride ions (negative ion) within the nanochannel networks[31, 61, 62] and it may bring the higher ion-selectivity. The ion-selectivity can be explained

by the ratio between the counter-ion and co-ion fluxes, which is denoted by $\eta = -J_+/J_-$ within the negatively charged NCNM.[52, 71, 72] For the perfect ion-selectivity, the factor of $(\eta+1)/(\eta-1) \to 1$ as $\eta \to \infty$. The limiting current, I_{lim}, and the threshold voltage, V_o, for this limiting current are in proportion to this ratio of $(\eta+1)/(\eta-1)$.[52, 71, 72] Therefore, reducing the nanoparticle size leads to the high ion selectivity and subsequently results in the low value of I_{lim} and V_o simultaneously with the rapid growth of the depletion layer (earlier onset time). Another reason of this is that the counter-ion concentration in the nanopores increases with the decrease of the diameter and it results in the higher conductivity, shown in **Fig. 3(b)**. Irrespective of the diameter of the nanoparticles, the close-packed nanoparticle with FCC structure has the same packing efficiency (volume of space occupied by the spheres/total volume) and its value is 74.05 % in this case. Therefore, if the nanoparticles are ideally self-assembled within the same volume of the shallow channel, the smaller diameter of the nanoparticles have larger surface area, which increases the ionic conductance.

However, there may have the limitation in increase of the ionic conductance and decrease of the onset time by reducing the size of nanoparticles. In case of the diameter of 100 nm, despite of the lowest value of $c_{0,r}^* h_n^*$ (~0.014) and the strongly cation-selective, the onset time turns higher and ionic current becomes lower. We believe that it is because of the enhancement of the electrical resistance of the NCNM by the physical confinement such as pure steric exclusion and hydrodynamic drag,[73-75] or tortuous interstitial spaces of the opal:[76] First, the increases of the ratio of the ion size to nanopore size can induce the hindrance. It means the smaller particle is more affected by physical confinement. Second, when the length of the NCNM, l_s, becomes longer, the number of these affected nanopores increases and also the tortuosity become increases. In our experimental condition where 200, 300, and 700 nm of the diameter with 400

μm of l_s, the effect of the counter-ion attraction from the surface charge density may still higher than these physical confinements. However, the effect of these hindrances at 400 μm of l_s may become significant at the diameter with 100 nm. Thus, the electrical resistance of the NCNM increases. From this point of view, if the nanoparticle has lower diameter than 100 nm, the length of the NCNM should be decreased for increase the ionic conductance and decrease the onset time.

Fig. 4(a) and (b) show the *I-V* curves and the onset time as the function of the width of the shallow channel, w_s, respectively. As can be expected, the currents become higher as w_s increases because of the increase in the electrical conductance of the NCNM ($K_{networks}$), *i.e.* $K_{networks} \propto w_s$.[52, 70] The onset time increases with decreasing w_s and, especially, the onset time increases dramatically below 100 μm of w_s (**Fig. 4(b)**) and the limiting current region is also vanished (**Fig. 4(a)**). It seems because of the corner vortex pairs by the induced charge electro-osmosis,[77-79] the combined field focusing, and/or the space charge effects.[46, 72] **Fig. S3 in ESI†** shows the sequential images of the depletion layer pattern evolution, confirming these possible explanations. When the ICP is triggered, the small-size pattern of periodic undulation of the depletion layers is formed. Subsequently, these small layers are merged into one large depletion layer and they expand over time. However, there still exist ejecting vortices which disturb the stability of the depletion layer at each side of the wall by the corner effects.[72] As shown in **Fig. 4(c)**, when w_s is sufficiently large ($w_s \rightarrow 400 \mu m$), the corner vortices occupy only a small portion of the entire entrance width and hence the depletion layer can stably grow with the existing limiting current region. On the contrary, for the narrower width of the shallow channel ($w_s \rightarrow 25 \mu m$), since these corner vortices become dominant, the mixing actions can allow the ion for transport through the NCNM of the entire entrance w_s by increasing the onset time and there

15

seems to be a direct transition to the overlimiting region without the limiting current region. Yossifon and co-workers[72] explained this disappearance of the limiting region at narrow w_s theoretically and experimentally: there should be severe ionic concentration gradients (effectively resulting in a much shorter depletion region) and the ejecting vortex pair is sustained by the enhanced field focusing at the point-like, narrow w_s.

We conducted the measurement of the onset time and *I-V* curves as the function of the height of the shallow channel (h_s), shown in **Fig. 5(a) and (b)**. When we trigger the ICP, the onset time tends to decrease as h_s becomes higher. It seems because, unlike the conventional nanochannel at adequately low concentration, $K_{networks}$ of the shallow channel increases and it leads to more counter-ion transport through the channel as heightening h_s. In the case of the conventional nanochannels (w_n: width, h_n: height, l_n: length of the nanochannel), the electrical conductance of the nanochannel (K_n) can be expressed as follows.[70] At a higher concentration, where $\lambda_D^{-1} h_n \gg 1$, K_n is $(10^3 \sum_i \mu_i c_i N_A e) \cdot w_n h_n / d_n$ that depends on the nanoaperture`s geometry and the bulk electrolyte concentration (λ_D is the Debye length,[67, 68] μ_i is the mobility of ion i, c_i is the concentration of ion i, N_A is the Avogadro constant, and e is the electron charge). At a low concentration, where $\lambda_D^{-1} h_n \ll 1$, an approximation is true, *i.e.* $K_n \approx 2|\sigma| \mu_{excess} w_n / l_n$, since an excess mobile counter-ion concentration (c_{excess}) in the nanochannel become dominant. Note that this value is independent on h_n and c_i, wherein $c_{excess} = 10^{-3} \{2|\sigma| /(h_s N_A e)\}$, σ is surface charge density, and μ_{excess} is the mobility of excess ion through the nanochannel. In the case of our shallow channel filled with the nanoparticles, we can approximately assume that these nanochannels were stacked by inter-connecting one another within the shallow channel. Consequently, the total excess ion concentration through the NCNM would increase as the

nanochannels are piled up over the height of the shallow channel (h_s). Therefore, the electrical conductance ($K_{networks}$) of the NCNM is in proportion not only to w_s but also to h_s unlike the conventional nanochannel at the low concentration ($\lambda_D^{-1} h_n \ll 1$). We thus have this relation $K_{networks} \propto A_s$ (wherein A_s is the cross sectional area of the shallow channel), and also $K_{networks}^* = A_s^* / l_s \cdot (\gamma_{bulk} + \gamma_{excess})$, overall. Here A_s^* is the effective cross sectional area of ideally-close-packed homogeneous nanoparticles into the FCC structure (21.50 % of A_s, more details in Sec. IV of ESI†) and l_s, γ_{bulk}, γ_{excess} are the length of the shallow channel, the bulk conductivity, and the surface conductivity contribution from the excess counter-ion through the NCNM, respectively.

We observed the ICP phenomena according to the surface charge of the nanoparticles by changing the pH value of the 0.1 mM KCl electrolyte. It is well known that the pH value of the electrolyte has a significant influence on the effective surface charge density of materials[69, 80, 81] and the electric conductance of nanochannels[52, 60, 70]. We changed the value of the pH by adding HCl for the acid and KOH for the base, and then measured the *I-V* curves (**Fig. 6(a),** blank symbol with the solid lines) for the NCNM constituted with the silica nanoparticles (S-NPs). As compared with the value of the pH 5.6, the electrical conductance increases when the value of the pH is 9.4 in the Ohmic regime. This trend is able to explain by improved surface charge density at pH 9.4. The aforementioned surface charge density of particle based on the full multi-ion charge regulation model, σ_A^*, can be determined by the implicit equation as

$$\sigma_B^* = 2\varepsilon\kappa R_g T z^{-1} F^{-1}[A]\{1 + 2d_n^{-1}\kappa^{-1}[B]^{-2} + 16(d_n\kappa)^{-2}\ln[B][A]^{-2}\}^{0.5}.$$ [65, 66] Here, Stern layer effect is neglected; ε is the permittivity of the electrolyte solutions (7.08×10^{-10} F·m^{-1}); z is the valence of the ions ($z = 1$); $\kappa^{-1} = \lambda_D = (\varepsilon R_g T / 2z^2 F^2 c_0)^{0.5}$ and bulk concentration, c_0, is $c_{KCl} + 10^{-pH}$ for

pH 5.6, wherein c_{KCl} is the concentration of the KCl (0.1 mM); [67, 68] $A = \sinh(zF\zeta / 2R_g T)$ and

$B = \cosh(zF\zeta / 2R_g T)$. When the value of the pH is 9.4, one can easily obtain change of the

surface charge density by adjusting the zeta potential from the equation, $\sigma_A^* = \sigma_B^*$.[66] As a result,

both the surface charge density and the zeta potential are increase at pH 9.4 and its value is -

0.05073 C·m^{-2} and 222 mV, respectively. This trend is consistent with the results of the pH

titration and the site-dissociation model for the silica or glass surface.[52, 69, 80, 81]

   As the pH values decrease further until pH 4.0, the ionic conductance of NCNM increases

dramatically, which contradictory to the aforementioned argument: the electrical conductance of

the NCNM should be lowered because the surface charge density of the nanoparticles is reduced

as the pH value decreases. We believe that it is because the bulk concentration of hydronium is

much higher than the KCl concentration of 0.1 mM in this case, $i.e.$ $c_{H^+} \gg c_{K^+}$. Jensen and co-

workers[60] theoretically and experimentally explained that the hydronium ion will be dominant

for the ion transport through the nanochannel if the sufficiently low concentration of salt

electrolyte with the lower pH value is used. That is, the contribution to change of conductivity in

the NCNM by the excessive hydronium ion concentration is much higher than it by the variation

of surface charge in low concentration of electrolyte. The detailed expression of the surface

conductivity   contribution   from   the   excess   counter-ion   is

$\gamma_{excess} \approx 2|\sigma|\{c_{K^+}\mu_{K^+}(c_{K^+} + c_{H^+})^{-1} + c_{H^+}\mu_{H^+}(c_{K^+} + c_{H^+})^{-1}\}$.[52, 70] Therefore, if $c_{H^+} \gg c_{K^+}$ is true,

γ_{excess} becomes $\sim 2|\sigma|\mu_{H^+}$ and it is noted that the conductivity is independent on the K$^+$ but

dependent on the hydronium (μ_i is the ion mobility of i-type ion). In addition, the lower pH

showed the higher conductance when the conductance for pH 4.0 is compared with the case of

pH 9.4, as shown in **Fig. 6(a)**. We can explain it by that the ion mobility of the hydronium (μ_{H^+}

) higher than the potassium (μ_{K^+}) promotes the excess ion concentration with the higher conductance into the NCNM ($\mu_{H^+} \approx 36.3 \times 10^{-8} m^2 V^{-1} s^{-1}$ and $\mu_{K^+} \approx 7.62 \times 10^{-8} m^2 V^{-1} s^{-1}$ in reference)[63, 64]. Our pH/conductivity measurement confirms it: the value was 62.9 µS/cm for the value of the pH 4.0 and 30.4 µS/cm for pH 9.4.

We investigated the effects of the surface properties by changing the material of the nanoparticle from the silica nanoparticles (S-NPs) to the polystyrene nanoparticles (PS-NPs) under the condition of 0.1 mM KCl. As shown in **Fig. 6(a),** $K_{networks}$ of the PS-NPs is greater than that of the S-NPs for all the values of pH in the Ohmic region. It can be explained by different surface properties, *i.e.* the hydrophilic (S-NPs) versus hydrophobic (PS-NPs) surfaces. The thin water depletion layer is known to be exhibited close to a hydrophobic surface and the viscosity of this layer (η_l) is assumed to be substantially lower than the bulk water viscosity (η_0). It results in amplifying the hydrodynamic slippage at solid surfaces, which is often quantified by the so-called slip length, b (usually few tens of nanometer).[82-85] The electro-osmotic ion mobility (μ_{EO}) can be simply described as $\mu_{EO} \approx \psi_0 (1 + b\lambda_D^{-1}) \cdot \eta_0^{-1}$,[83, 86] and $b = t \cdot (\eta_0 \eta_l^{-1} - 1)$,[84] where t is a thickness of depletion water layer close to the nanoparticle surface. On the S-NPs having a hydrophilic surface, the slip length can be neglected since η_l is approximately equal to η_o. In contrast, on the PS-NPs having hydrophobic surfaces ($\eta_0 \gg \eta_l$), the slip length is finite, μ_{EO} becomes amplified at the NCNM, and this amplified ion mobility results in high ion flux and the subsequent increase of $K_{networks}$.

Fig. 6(b) shows the comparison of the onset time between the NCNM consisting with the S-NPs and the PS-NPs at different pH values. Indeed, it is hard to directly compare the results among different pH values for the same material because the FITC exists in different ionic states inside aqueous solutions of various pH values.[87-89] In a neutral or a weakly acidic condition, the

fluorescein has the neutral, the anionic, and the di-anionic protolytic forms and thus the FITC is generally used to represent the depletion motion of the anions in the KCl electrolyte for the ICP phenomena[4, 24, 26] ($\mu_{Cl^-} \approx 7.19 \times 10^{-8} \, m^2 V^{-1} s^{-1}$ and $\mu_{fluorescei\ n} \approx 3 \sim 4 \times 10^{-8} \, m^2 V^{-1} s^{-1}$ in references)[64, 69, 90, 91]. However, at the further acidic pH with its lower value, the fluorescein no more represents the Cl⁻ motion because an anion and a di-anion form of the fluorescein is dramatically reduced. For this reason, the onset time has the largest value despite of the highest $K_{networks}$ at pH 4.0. There exists a clear distinction for the same value of the pH between the two different materials that we used: the PS-NPs case (filled vertical plots) shows a shorter onset time than the S-NPs case (blank vertical plots) because of its higher $K_{networks}$.

Finally, we investigate the ICP phenomena near the NCNM formed with self-assembled titanium dioxide nanoparticles (T-NPs). It is well known that different kinds of surface charges on the titanium dioxide (TiO_2) surface are induced in an aqueous environment depending on the values of pH. The surface charge is positive in acidic conditions (pH $\leq$ 5, due to the presence of the $\equiv TiOH_2^+$ groups), near-neutral between pH of 5 and 7, and negative in basic conditions (pH $\geq$ 7, due to the $\equiv TiO^-$ groups).[92, 93] The T-NPs that we used in this experiment are positively charged at pH $\leq$ 4.5 and negatively charged at pH $\geq$ 5. Accordingly, the NCNM becomes the anion-exchange membranes at the pH value of 4.0. **Fig. 7(a)** thus shows that the ion depletion region is established with the negative DC triggered since we used the cationic Rhodamine 6G chloride (R6G, $\mu_{R6G} \approx 1 \times 10^{-8} \, m^2 V^{-1} s^{-1}$)[91]. When the positive DC is applied and the negatively charged FITC solution with pH of 9.1 is used, the ion depletion layer is also established by its negative value of the zeta potential (cation selective), as shown in **Fig. 7(b)**.

CONCLUSION

We propose a microplatform having tunable 3D nanochannel networks constructed by the spatially controlled nanoparticle assembly in a cost effective and simple fashion. We also studied the electrokinetic characterization closely related with the scale, geometry, materials, and medium condition. Although nanopores and nanochannels has been studied in the previous works, there were clear challenging issues limited by the fabrication process, such as low ionic flux, high fluidic resistance, retarding the ion transport, and the confined materials. The aforementioned problems could be overcome successfully by the proposed NCNM consisting of the collective three-dimensional nanochannel networks. We believe that the proposed system showed a great flexibility for controlling ionic flux, limiting current region, and even changing the polarity of surface charge by designing the geometry of the microchannel and by selecting the size and materials of nanoparticles and the pH value of the solution. This can be even further improved performance in the future and contributes to extending applications using nanoscale electrokinetics, which have been limited by low ionic flux. For example, high power energy generation, high throughput biomolecule separation, purification and analysis can be realized in the near future. The characterization of the proposed NCNM proved that this system can be a new standard microplatform to study the mechanism of ion transport at nanoscale.
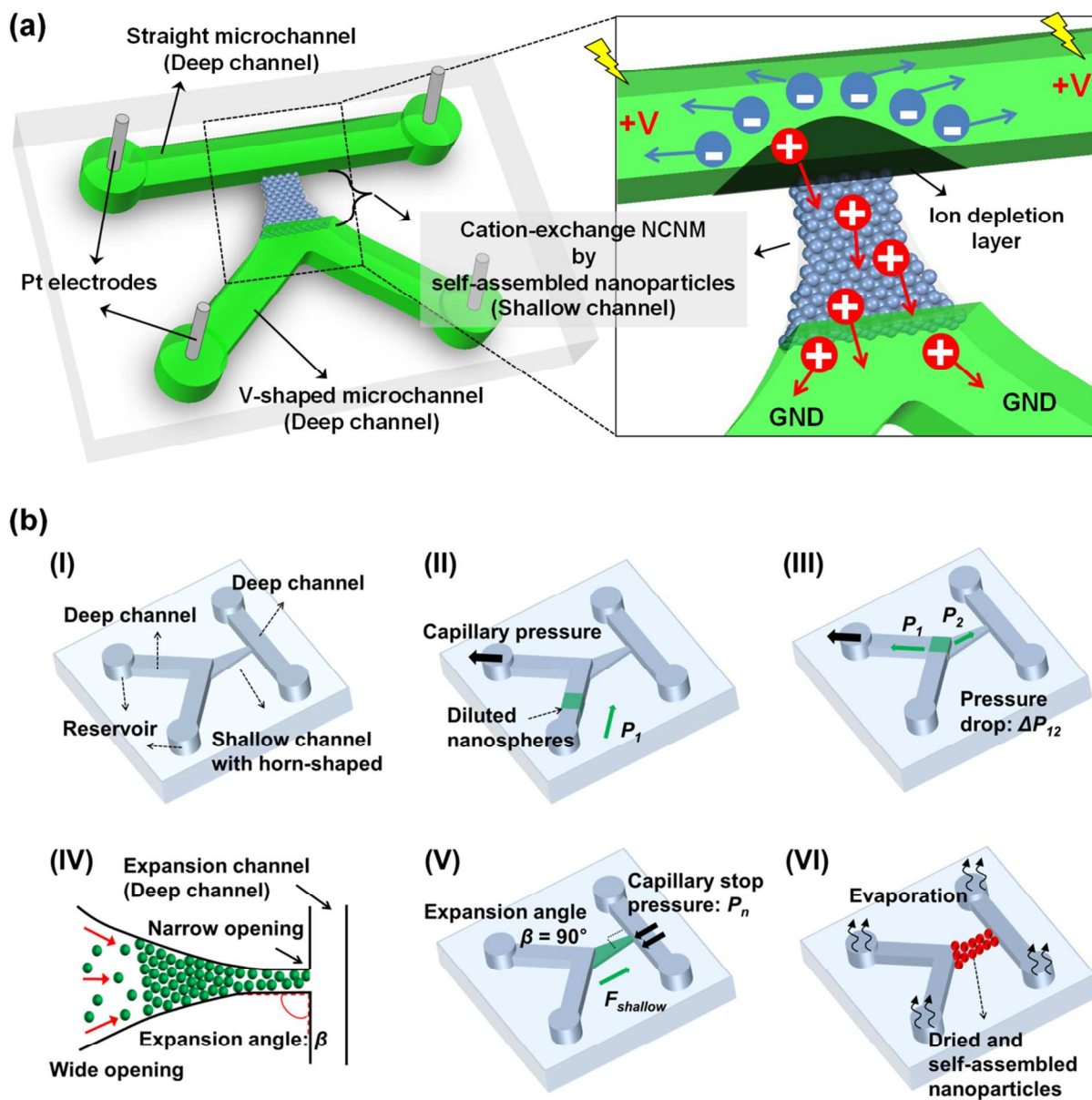
Fig. 1 (a) Schematic illustration of the proposed microplatform and the working principle of the ICP phenomenon. (b) Fabrication process for the *in situ* formation of nanochannel networks using the self-assembly of nanoparticles within the PDMS channel.

23
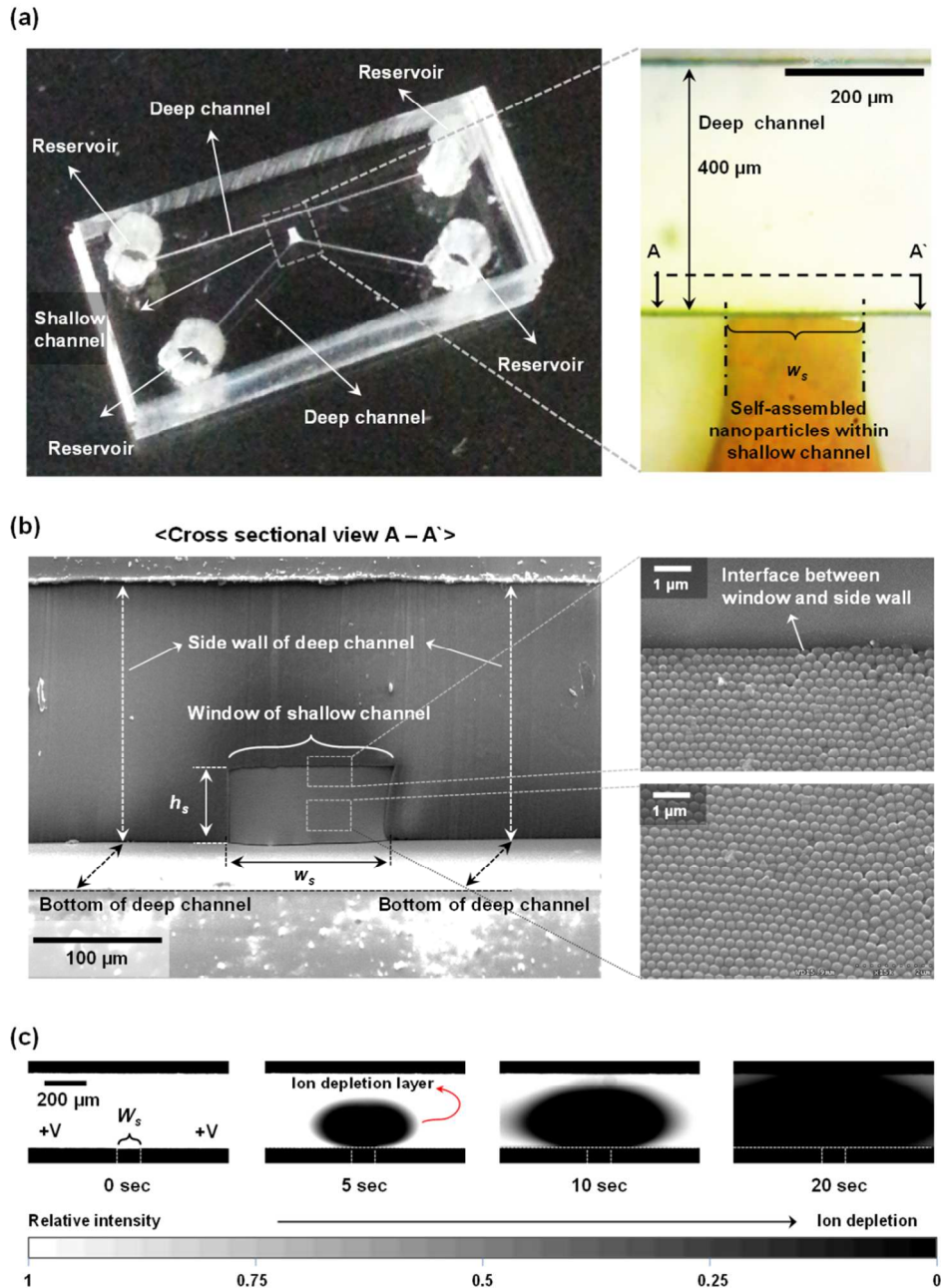
Fig. 2 (a) Fabricated microplatform and its enlarged microscopic images where the interface between the shallow and the deep channels. (b) SEM images of the fabricated device at cross-section in the direction of A-A` (left) and its enlarged image of the interface between the window of shallow channel and the side wall of the deep channel, and the middle of the window of the shallow channel (right). (c) Fluorescent images of the ion depletion region as the function of time.
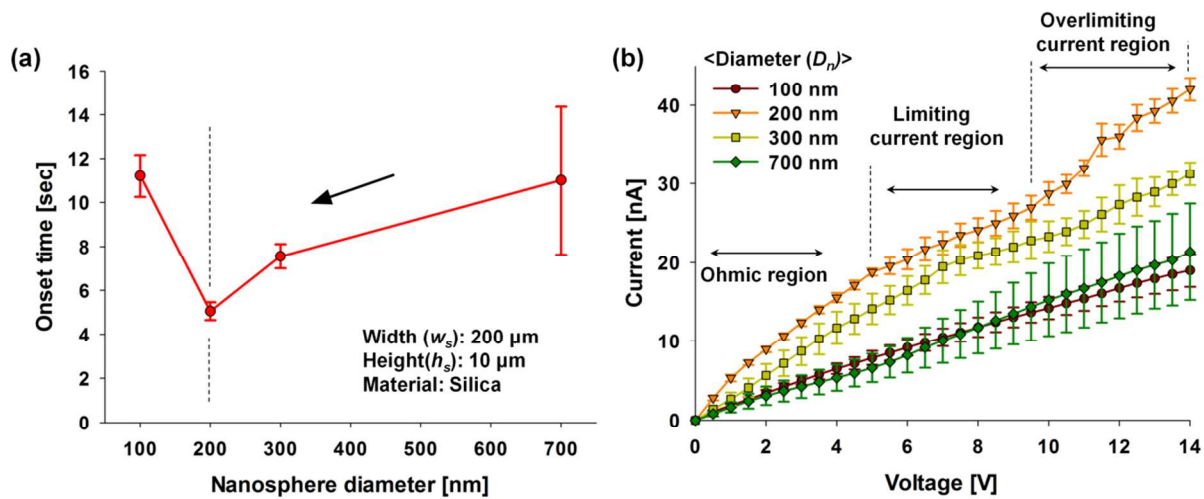
Fig. 3 (a) Change in the onset time with varying diameters of the nanoparticles. (b) *I-V* characteristics of NCNM with varying diameters of the nanoparticles.
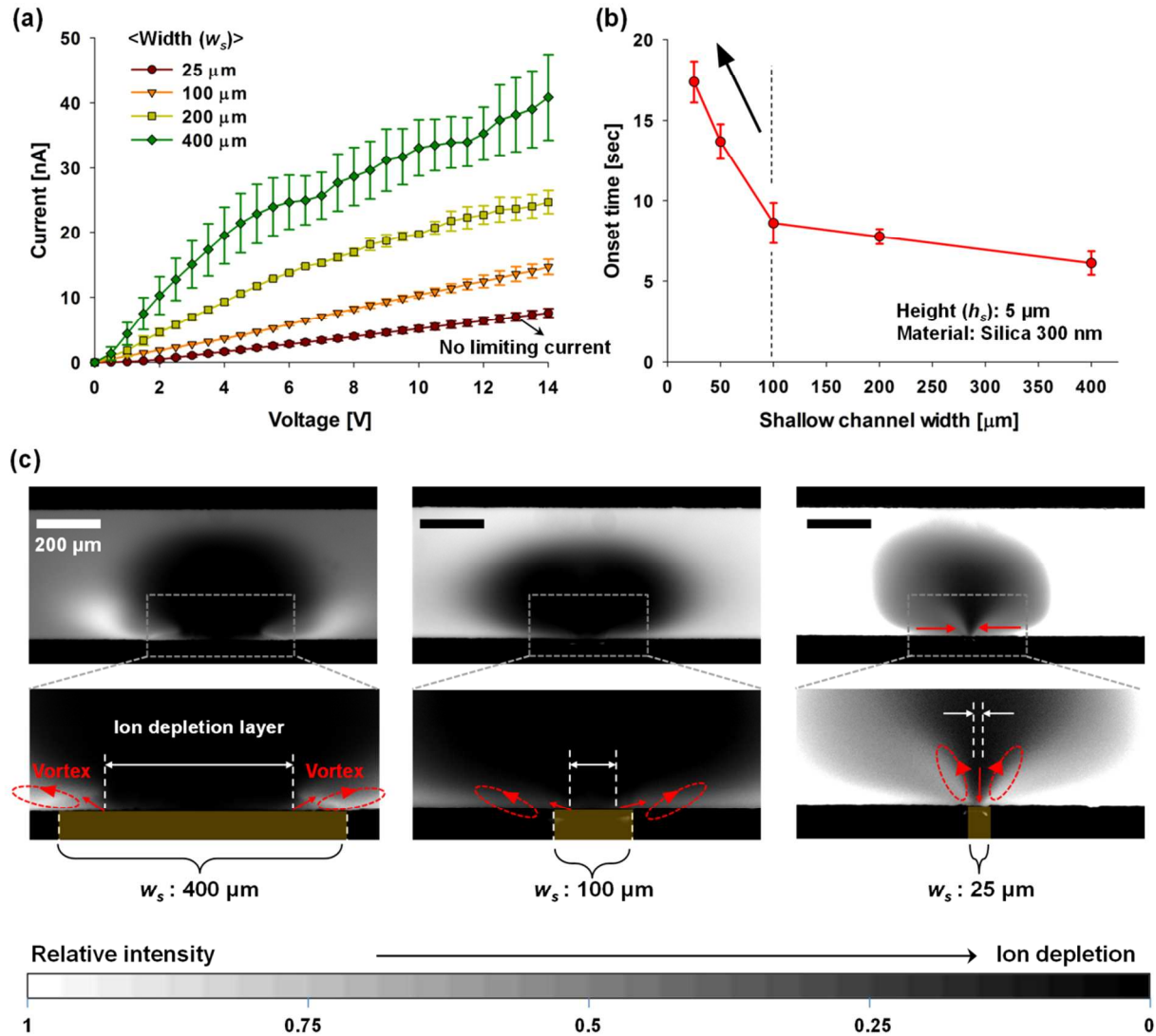
Fig. 4 (a) *I-V* characteristics of the NCNM with varying widths of the shallow channel. (b) Change in the onset time with varying widths of the shallow channel. (c) Fluorescent image of the ion depletion region and the corner vortices at each side wall of the NCNM as a function of the width of the shallow channel.
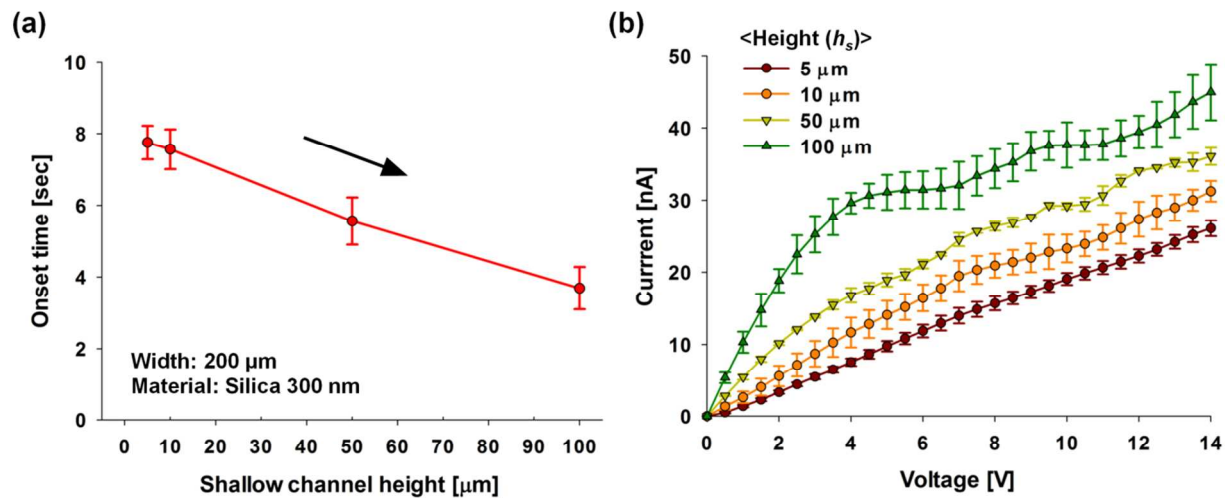
Fig. 5 (a) Change in the onset time with varying heights of the shallow channel. (b) *I-V* characteristics of NCNM with varying heights of the shallow channel.

27
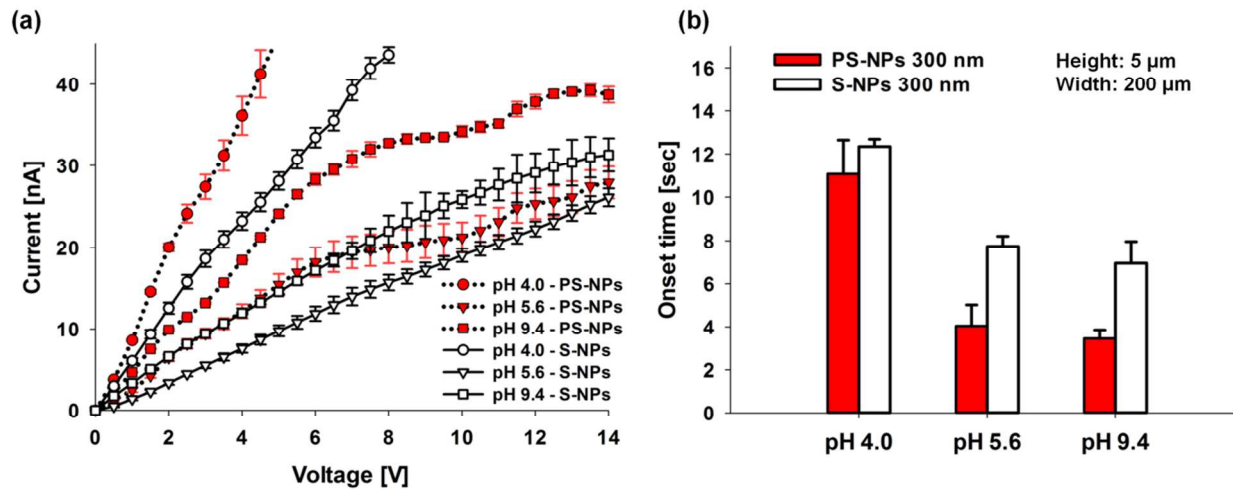
Fig. 6 (a) *I-V* characteristics of NCNM with varying values of the pH and the materials of the nanoparticles (silica nanoparticles (S-NPs) and polystyrene nanoparticles (PS-NPs)). (b) Comparison of the onset time between the NCNM consisted with S-NPs and PS-NPs different pH values.

28

(a)

pH: 4.2, Anion-exchange NCNM, R6G (Positively charged)

200 μm

w_s : 200 μm

- V   - V

0 sec   15 sec   30 sec   40 sec

Relative intensity   Ion depletion

1   0.75   0.5   0.25   0

(b)

pH: 9.1, Cation-exchange NCNM, FITC (Negatively charged)

200 μm

w_s : 200 μm

+ V   + V

0 sec   3 sec   9 sec   27 sec

Relative intensity   Ion depletion

1   0.75   0.5   0.25   0

Fig. 7 ICP phenomena near the NCNM formed with the self-assembled titanium dioxide nanoparticles (T-NPs) with varying the pH value at (a) 4.2 and (b) 9.1.

REFERENCES

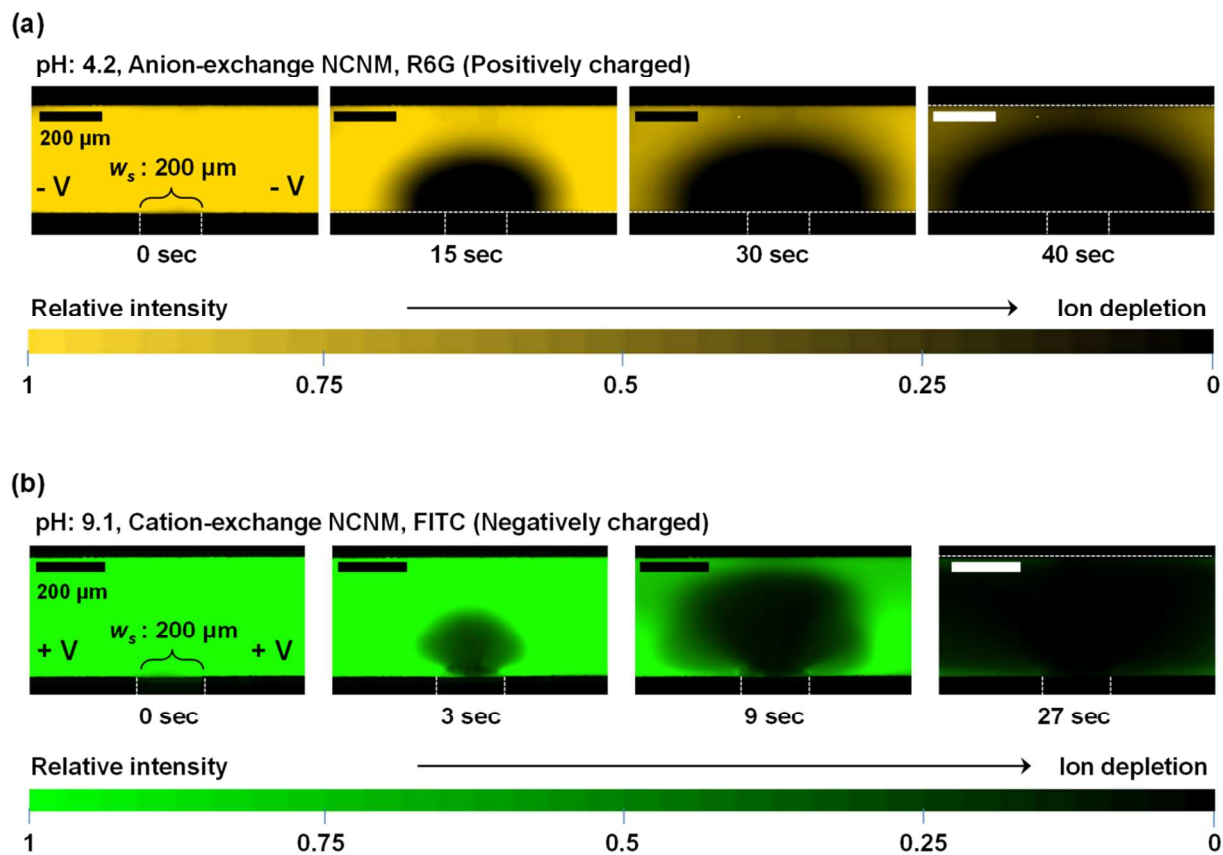1.   P. Mao and J. Y. Han, *Lab chip*, 2005, 5, 837-844.

2.   R. Chantiwas, S. Park, S. A. Soper, B. C. Kim, S. Takayama, V. Sunkara, H. Hwang and Y.-K. Cho, *Chem. Soc. Rev.*, 2011, 40, 3677-3702.

3.   S. J. Kim, Y. A. Song and J. Han, *Chem. Soc. Rev.*, 2010, 39, 912-922.

4.   H. C. Chang, G. Yossifon and E. A. Demekhin, *Annu. Rev. Fluid Mech.*, 2012, 44, 401-426.

5.   S. J. Lee and D. Kim, *Microfluid. Nanofluid.*, 2012, 12, 897-906.

6.   D. Kim, A. Raj, L. Zhu, R. I. Masel and M. A. Shannon, *Lab chip*, 2008, 8, 625-628.

7.   D.-K. Kim, C. Duan, Y.-F. Chen and A. Majumdar, *Microfluid. Nanofluid.*, 2010, 9, 1215-1224.

8.   W. Guo, L. X. Cao, J. C. Xia, F. Q. Nie, W. Ma, J. M. Xue, Y. L. Song, D. B. Zhu, Y. G. Wang and L. Jiang, *Adv. Funct. Mater.*, 2010, 20, 1339-1344.

9.   L. X. Cao, W. Guo, W. Ma, L. Wang, F. Xia, S. T. Wang, Y. G. Wang, L. Jiang and D. B. Zhu, *Energy Environ. Sci.*, 2011, 4, 2259-2266.

10.   K. Schmidt-Rohr and Q. Chen, *Nat. Mater.*, 2008, 7, 75-83.

11.   S. Liu, Q. Pu, L. Gao, C. Korzeniewski and C. Matzke, *Nano Lett.*, 2005, 5, 1389-1393.

12.   K. Kwon, S. J. Lee, L. Li, C. Han and D. Kim, *Int. J. Energ. Res.*, 2014, 38, 530-537.

13.   M. Kim, M. Jia and T. Kim, *Analyst*, 2013, 138, 1370-1378.

14.   S. H. Ko, Y.-A. Song, S. J. Kim, M. Kim, J. Han and K. H. Kang, *Lab chip*, 2012, 12, 4472-4482.

15.   J. Han and H. G. Craighead, *Science*, 2000, 288, 1026-1029.

16.   S. J. Kim, S. H. Ko, K. H. Kang and J. Han, *Nat. Nanotechnol.*, 2013, 8, 609-609.

17.   H. Daiguji, Y. Oka and K. Shirono, *Nano Lett.*, 2005, 5, 2274-2280.

18.   I. Vlassiouk and Z. S. Siwy, *Nano Lett.*, 2007, 7, 552-556.

19.   S. J. Kim, S. H. Ko, R. Kwak, J. D. Posner, K. H. Kang and J. Han, *Nanoscale*, 2012, 4, 7406-7410.

20.   J. Balster, M. H. Yildirim, D. F. Stamatialis, R. Ibanez, R. G. H. Lammertink, V. Jordan and M. Wessling, *J. Phys. Chem. B*, 2007, 111, 2152-2165.

21.   N. D. Pismenskaya, V. V. Nikonenko, E. I. Belova, G. Y. Lopatkova, P. Sistat, G. Pourcelly and K. Larshe, *Russ. J. Electrochem.*, 2007, 43, 307-327.

22.   E. I. Belova, G. Y. Lopatkova, N. D. Pismenskaya, V. V. Nikonenko, C. Larchet and G. Pourcelly, *J. Phys. Chem. B*, 2006, 110, 13458-13469.

23.   D. Hlushkou, R. Dhopeshwarkar, R. M. Crooks and U. Tallarek, *Lab chip*, 2008, 8, 1153-1162.

24.   P. Kim, S. J. Kim, J. Han and K. Y. Suh, *Nano Lett.*, 2010, 10, 16-23.

25.   R. S. Foote, J. Khandurina, S. C. Jacobson and J. M. Ramsey, *Anal. Chem.*, 2005, 77, 57-63.

26.   S. J. Kim, Y. C. Wang, J. H. Lee, H. Jang and J. Han, *Phys. Rev. Lett.*, 2007, 99, 044501.

27.   A. Plecis, R. B. Schoch and P. Renaud, *Nano Lett.*, 2005, 5, 1147-1155.

28.   C. H. Duan and A. Majumdar, *Nat. Nanotechnol.*, 2010, 5, 848-852.

29.   A. Piruska, S. P. Branagan, A. B. Minnis, Z. Wang, D. M. Cropek, J. V. Sweedler and P. W. Bohn, *Lab chip*, 2010, 10, 1237-1244.

30.   S. A. Miller, K. C. Kelly and A. T. Timperman, *Lab chip*, 2008, 8, 1729-1732.

31.   T. A. Zangle, A. Mani and J. G. Santiago, *Chem. Soc. Rev.*, 2010, 39, 1014-1035.

32.   G. Yossifon, Y. C. Chang and H. C. Chang, *Phys. Rev. Lett.*, 2009, 103.

33.   J. L. Perry and S. G. Kandlikar, *Microfluid. Nanofluid.*, 2006, 2, 185-193.

34.   D. C. Martins, V. Chu and J. P. Conde, *Biomicrofluidics*, 2013, 7.

35.   E. Choi, H. K. Chang, C. Y. Lim, T. Kim and J. Park, *Lab chip*, 2012, 12, 3968-3975.

36.   Z. Chen, Y. S. Wang, W. Wang and Z. H. Li, *Appl. Phys. Lett.*, 2009, 95.

37.   Y. Zeng and D. J. Harrison, *Anal. Chem.*, 2007, 79, 2289-2295.

38.   Q. S. Pu, J. S. Yun, H. Temkin and S. R. Liu, *Nano Lett.*, 2004, 4, 1099-1103.

39.   A. S. Khair, *Phys. Fluids*, 2011, 23.

40.   I. Rubinstein, B. Zaltzman and O. Kedem, *J. Membr. Sci.*, 1997, 125, 17-21.

41.   I. Rubinstein and B. Zaltzman, *Phys. Rev. E*, 2000, 62, 2238-2251.

42.   I. Rubinstein and B. Zaltzman, *Phys. Rev. E*, 2003, 68.

43.   I. Rubinstein, B. Zaltzman and I. Lerman, *Phys. Rev. E*, 2005, 72.

44.   S. M. Rubinstein, G. Manukyan, A. Staicu, I. Rubinstein, B. Zaltzman, R. G. Lammertink, F. Mugele and M. Wessling, *Phys. Rev. Lett.*, 2008, 101, 236101.

45.   S. S. Dukhin and B. V. Derjaguin, *Electrophoresis*, Nauka, Moscow, 1976.

46.   S. S. Dukhin, *Adv. Colloid Interface Sci.*, 1991, 35, 173-196.

47.   S. S. Dukhin and N. A. Mishchuk, *J. Membr. Sci.*, 1993, 79, 199-210.

48.   N. A. Mishchuk and P. V. Takhistov, *Colloids Surf. Physicochem. Eng. Aspects*, 1995, 95, 119-131.

49.   E. M. Egorova, *Electrophoresis*, 1995, 16, 905-910.

50.   S. Chung, H. Yun and R. D. Kamm, *Small*, 2009, 5, 609-613.

51.   K. H. Chung, J. W. Hong, D. S. Lee and H. C. Yoon, *Anal. Chim. Acta*, 2007, 585, 1-10.

52.   C. C. Chang, C. P. Yeh and R. J. Yang, *Electrophoresis*, 2012, 33, 758-764.

53.   I. Rubinstein and L. Shtilman, *J. Chem. Soc., Faraday Trans. 2*, 1979, 75, 231-246.

54.   Y. Tanaka and M. Seno, *J. Chem. Soc., Faraday Trans. 1*, 1986, 82, 2065-2077.

55.   Y. Tanaka, *J. Membr. Sci.*, 2002, 203, 227-244.

56.   Y. Tanaka, *Russ. J. Electrochem.*, 2012, 48, 665-681.

57.   A. Persat, M. E. Suss and J. G. Santiago, *Lab chip*, 2009, 9, 2454-2469.

58.   M. Macka, P. Andersson and P. R. Haddad, *Anal. Chem.*, 1998, 70, 743-749.

59.   A. Persat, R. D. Chambers and J. G. Santiago, *Lab chip*, 2009, 9, 2437-2453.

60.   K. L. Jensen, J. T. Kristensen, A. M. Crumrine, M. B. Andersen, H. Bruus and S. Pennathur, *Phys. Rev. E*, 2011, 83.

61.   T. A. Zangle, A. Mani and J. G. Santiago, *Langmuir*, 2009, 25, 3909-3916.

62.   A. Mani, T. A. Zangle and J. G. Santiago, *Langmuir*, 2009, 25, 3898-3908.

63.   T. Okada, H. Satou, M. Okuno and M. Yuasa, *J. Phys. Chem. B*, 2002, 106, 1267-1273.

64.   S. Koneshan, J. C. Rasaiah, R. M. Lynden-Bell and S. H. Lee, *J. Phys. Chem. B*, 1998, 102, 4193-4204.

65.   L. H. Yeh, S. Xue, S. W. Joo, S. Qian and J. P. Hsu, *J. Phys. Chem. C*, 2012, 116, 4209-4216.

66.   S. Atalay, Y. Ma and S. Z. Qian, *J. Colloid Interface Sci.*, 2014, 425, 128-130.

67.   S. Xue, L. H. Yeh, Y. Ma and S. Z. Qian, *J. Phys. Chem. C*, 2014, 118, 6090-6099.

68.   M. Barisik, S. Atalay, A. Beskok and S. Z. Qian, *J. Phys. Chem. C*, 2014, 118, 1836-1842.

69.   M. B. Andersen, J. Frey, S. Pennathur and H. Bruus, *J. Colloid Interface Sci.*, 2011, 353, 301-310.

70.   R. B. Schoch and P. Renaud, *Appl. Phys. Lett.*, 2005, 86.

71.   G. Yossifon, P. Mushenheim, Y. C. Chang and H. C. Chang, *Phys. Rev. E*, 2009, 79.

72.   G. Yossifon, P. Mushenheim, Y. C. Chang and H. C. Chang, *Phys. Rev. E*, 2010, 81.

73.   J. Y. Han, J. P. Fu and R. B. Schoch, *Lab chip*, 2008, 8, 23-33.

74.   V. V. Swaminathan, L. R. Gibson, M. Pinti, S. Prakash, P. W. Bohn and M. A. Shannon, *J. Nanopart. Res.*, 2012, 14.

75.   E. M. Renkin, *J. Gen. Physiol.*, 1954, 38, 225-243.

76.   M. R. Newton, K. A. Morey, Y. H. Zhang, R. J. Snow, M. Diwekar, J. Shi and H. S. White, *Nano Lett.*, 2004, 4, 875-880.

77.   Y. Eckstein, G. Yossifon, A. Seifert and T. Miloh, *J. Colloid Interface Sci.*, 2009, 338, 243-249.

78.   G. Yossifon, I. Frankel and T. Miloh, *Phys. Fluids*, 2006, 18, -.

79.   S. K. Thamida and H.-C. Chang, *Phys. Fluids*, 2002, 14, 4315-4328.

80.   S. H. Behrens and D. G. Grier, *J. Chem. Phys.*, 2001, 115, 6716-6721.

81.   I. Altug and M. L. Hair, *J. Phys. Chem.*, 1967, 71, 4260-4263.

82.   D. M. Huang, C. Sendner, D. Horinek, R. R. Netz and L. Bocquet, *Phys. Rev. Lett.*, 2008, 101.

83.   C. I. Bouzigues, P. Tabeling and L. Bocquet, *Phys. Rev. Lett.*, 2008, 101.

84.   C. Sendner, D. Horinek, L. Bocquet and R. R. Netz, *Langmuir*, 2009, 25, 10768-10781.

85.   J. Servantie and M. Muller, *Phys. Rev. Lett.*, 2008, 101.

86.   L. Joly, C. Ybert, E. Trizac and L. Bocquet, *Phys. Rev. Lett.*, 2004, 93.

87.   M. M. Martin and L. Lindqvist, *J. Lumin.*, 1975, 10, 381-390.

88.   L. Cole, J. Coleman, D. Evans and C. Hawes, *J. Cell Sci.*, 1990, 96, 721-730.

89.   R. Sjoback, J. Nygren and M. Kubista, *Spectrochim. Acta. A. Mol. Biomol. Spectrosc.*, 1995, 51, L7-L21.

90.   S. A. Smith and W. A. Pretorius, *Water SA*, 2002, 28, 395-402.

91.   D. Milanova, R. D. Chambers, S. S. Bahga and J. G. Santiago, *Electrophoresis*, 2011, 32, 3286-3294.

92.   H. Park and W. Choi, *J. Phys. Chem. B*, 2005, 109, 11667-11674.

93.   M. R. Hoffmann, S. T. Martin, W. Y. Choi and D. W. Bahnemann, *Chem. Rev.*, 1995, 95, 69-96.